


Single and double charge transfer in the $\text{Ne}^{2+} + \text{He}$ collision within time-dependent density-functional theory

Wandong Yu ^{1,2} Cong-Zhang Gao ^{3,*} Shunsuke A. Sato ^{4,5} Alberto Castro ^{6,7,†} Angel Rubio ⁵ and Baoren Wei^{1,2,‡}

¹*Institute of Modern Physics, Department of Nuclear Science and Technology, Fudan University, Shanghai 200433, China*

²*Key Laboratory of Nuclear Physics and Ion-beam Application (MOE), Fudan University, Shanghai 200433, China*

³*Institute of Applied Physics and Computational Mathematics, Beijing 100088, China*

⁴*Center for Computational Sciences, University of Tsukuba, 1-1-1 Tennodai, Tsukuba, Ibaraki, Japan*

⁵*Max Planck Institute for the Structure and Dynamics of Matter, Luruper Chaussee 149, 22761 Hamburg, Germany*

⁶*ARAID Foundation, 50018 Zaragoza, Spain*

⁷*Institute for Biocomputation and Physics of Complex Systems, University of Zaragoza, Calle Mariano Esquillor, 50018 Zaragoza, Spain*



(Received 30 October 2020; accepted 15 February 2021; published 12 March 2021)

We calculate the charge-transfer cross sections for the $\text{Ne}^{2+} + \text{He}$ collision. To this end, we employ Ehrenfest molecular dynamics with time-dependent density-functional theory. The active electrons of the projectile are handled by applying an initial velocity to the Kohn-Sham orbitals via a Galilean boost. The dynamical calculations are performed in an inverse collision framework—the reference frame considers Ne^{2+} to be initially at rest, which ensures numerically converged final-time scattering states. The charge-transfer probabilities are extracted by extending the particle number projection technique to be able to handle the degenerate Ne^{2+} ion. Compared with experimental data available at 10–3000 keV, a fairly good agreement is found for the calculated single- and double-charge transfer cross sections, superior to other theoretical calculations for this $\text{Ne}^{2+} + \text{He}$ collision. A time-resolved analysis of the charge-transfer probabilities finds that ionization to the continuum also takes place after the charge transfer has occurred. To account for it, the final scattering states should be followed for a long time, approximately 350 fs, until they stabilize.

DOI: [10.1103/PhysRevA.103.032816](https://doi.org/10.1103/PhysRevA.103.032816)

I. INTRODUCTION

When a projectile ion collides with an atomic or molecular target at low-to-intermediate energies, a charge-transfer process usually occurs. It has been extensively studied for a wide variety of ion-atom–molecule systems, both experimentally and theoretically (for a recent review, see Ref. [1]). In experiments, the ion beam can be prepared by ionizing multi-electron atoms, thereby resulting in fully (*bare*) or partially stripped (*nonbare*) ions. While collisions with bare ions have been studied very often due to their simplicity [2,3], collisions with nonbare ions can be more complex and interesting. It was reported in Refs. [4–6], for example, that charge transfer is rather sensitive to the projectile's charge state, due to the change of the Coulomb field, which can even cause charge-transfer cross sections of nonbare and bare projectiles to vary by orders of magnitude. Nonbare projectiles play a role in a multitude of electronic and structural dynamics processes. Clear evidences of the impact of the active electrons of the projectiles have been found in several experiments, typically in the measurements of (state-selective) cross sections [7–9] and more recently in the momentum distributions of the recoil ions [10].

The description of the electronic screening effects of the projectile ion is essential for the theoretical modeling of nonbare ion collisions. In this context, the most straightforward scheme is to utilize a model potential. For instance, using the classical trajectory Monte Carlo (CTMC) method combined with a Coulomb-like screening potential, Olson *et al.* calculated charge-transfer cross sections for B^{q+} , C^{q+} , N^{q+} , and O^{q+} ions (here q stands for the charge state with $q \geq 3$) in collisions with the H atom in the 20–260 keV/amu [11] energy range. Within the Thomas-Fermi-type model potential, state-selective charge-transfer cross sections were also reported for nonbare Fe and Ne ions colliding with H [12,13].

The model potential method, however, may not be applicable at low collision energies due to its disregard of many-electron quantum effects. In this regime, alternative methods based on the independent electron approximation (IEA) have been applied with some success. In this regard, Kirchner and coworkers proposed a coupling mean-field approach, accounting for initial electron states with the IEA model [14]. It has been applied to study electron capture and/or ionization in certain nonbare ion collisions, e.g., $\text{C}^{3+} + \text{Ne}$ [15], $\text{He}^+ + \text{Ne}$ or Ar [16,17], B^{2+} or $\text{C}^{3+} + \text{Ne}$ [18], and $\text{He}^+ + \text{H}_2\text{O}$ [19]. By adding a screening potential to the Hamiltonian, the mean-field method was employed to investigate electron capture in the $\text{He}^+ + \text{He}$ collision [20]. Below 200 keV, the molecular-orbital close-coupling (MOCC) method was used to study $\text{Ne}^{2+} + \text{He}$ collisions [21], based on potential-energy curves and their coupling

*czgao88@hotmail.com

†acastro@bifi.es

‡brwei@fudan.edu.cn

matrix. The single-charge transfer cross sections agree well with measured data, but the double-charge transfer results deviate substantially. At high energies, the continuum-distorted-wave (CDW) method was validated to show a dependence of electron capture on the electronic states of the projectile [22,23].

Due to its computational efficiency and size scalability, the time-dependent density-functional theory (TDDFT) [24,25], together with nonadiabatic Ehrenfest dynamics, was the method of choice for a number of previous studies to simulate ionic projectile collisions with atomic, molecular, and solid targets [26–32]. In most cases, the projectile ion was either fully stripped (e.g., H^+ or He^{2+}) or at least stripped of all its valence electrons (e.g., C^{4+} and Ar^{8+}), such that the external potential could be simply modeled as a perturbed Coulomb field. However, the same treatment cannot be used for partially stripped ions, e.g., He^+ , C^{2+} , and Ar^{6+} , because the active projectile electrons (usually the valence electrons) may behave in a complex way: for example, they cannot tightly follow the nucleus during the collision, resulting in a projectile electric-dipole moment. This decoupling effect can be substantially enhanced when increasing the impact energy and/or increasing the number of active electrons of the projectile ion.

It is our goal in this paper to extend the TDDFT-Ehrenfest approach for the practical description of nonbare projectile ion collisions. We show an improved theoretical scheme that is adequate to yield predictive results in rather good agreement with experiments. To validate our method, we consider the $^{20}Ne^{2+} + ^4He$ collisions in the 10–3000 keV energy region (where this energy is defined to be the kinetic energy of the $^{20}Ne^{2+}$ ion, considering He to be initially at rest). To the best of our knowledge, for this process, the charge-transfer process and relevant cross sections spanning such region has yet to be theoretically studied at a quantitative level.

Specifically, (1) to account for the initial velocity of the electrons, we initially “boost” the Kohn-Sham (KS) orbitals by applying a phase transformation. This is unnecessary when dealing with bare ions. (2) An inverse collision framework is employed: we set the reference frame in which the He atom is the projectile that impacts the Ne^{2+} target. This choice has proven to be more robust and reliable, since the final electronic orbitals of the Ne ion can be propagated for a long time. (3) We extended the particle number projector (PNP) technique [33–35] to deal with fractionally occupied orbitals and analyzed the influence of ionization on charge-transfer probabilities. This extension was done within the spin-unrestricted version of KS TDDFT, and therefore it allows us to deal with arbitrary spin configurations for both projectile and target. This may be important because these processes are likely to depend on the initial spin states. (4) We used an efficient exponential representation of the PNP based on projection operator theory, as suggested in Refs. [34,36], to extract the probabilities. (5) We chose to test the simple adiabatic local density approximation (ALDA) [37] for this study. While this functional notoriously fails for the calculation of charge-transfer excitations, the results below—as well as other calculations (see Refs. [26,38] and other references therein)—show that the transfer induced by fast collisions, described in real-time, can be captured by the ALDA. The extension of this type

of studies to lower collision energies is a likely route for the benchmarking of functionals (see, for example, Ref. [39], where other frequently used xc functionals are discussed at low impact energies). A relevant question, for example, would be the effect of the self-interaction error present in the LDA and in other common functionals. This error leads to a too low highest single-particle eigenvalue, which should be, in exact DFT, equal to the ionization potential. However, the LDA ionization potentials computed as the total-energy differences between the neutral and charged species and that removed the outmost electron [40], are relatively good (for example in the case of He and Ne^+ , the errors are 2.04% and 1.80% compared with experimental values, respectively).

This article is organized as follows: Section II briefly recalls the TDDFT-Ehrenfest model. We also discuss the modifications that are required to deal with electrons that have a nonzero initial velocity. The extraction of charge-transfer probabilities is described in detail. In Sec. III, we present the computed charge-transfer cross sections, and we compare them with experimental and other calculated data. We furthermore inspect the impact-parameter-dependent electron-capture probabilities and show the impact of ionization on the charge transfer. Conclusions are finally drawn in Sec. IV.

II. THEORETICAL MODEL

A. Time-dependent density-functional theory together with Ehrenfest dynamics

The ion-atom-molecule collisions were modeled by using the TDDFT-Ehrenfest model [41]: the electrons are described with TDDFT and are nonadiabatically coupled to the nuclei, which are considered to be classical point particles. In practice, the propagation of an N -electron system is performed by making use of N single-particle wave functions (the Kohn-Sham orbitals, KSOs) $\{\psi_j, j = 1, 2, \dots, N\}$ governed by the time-dependent Kohn-Sham (TDKS) equations. The nuclear motion is described by the spatial coordinates of nuclei $\{\mathbf{R}_I, I = 1, 2, \dots, N_{\text{ion}}\}$ (N_{ion} stands for the number of nuclei) which is driven by the Coulomb force due to the presence of both the electrons and the other ions. In summary, the model consists of the following set of coupled equations (atomic units are used hereafter):

$$i \frac{\partial \psi_j(\mathbf{r}\sigma, t)}{\partial t} = \left[-\frac{1}{2} \nabla^2 + V_H[\rho](\mathbf{r}, t) + V_{xc}[\rho](\mathbf{r}, t) + V_{\text{en}}(\mathbf{r}, \{\mathbf{R}(t)\}) \right] \psi_j(\mathbf{r}\sigma, t), \quad (1)$$

$$M_I \frac{d^2 \mathbf{R}_I(t)}{dt^2} = -\nabla_{\mathbf{R}_I} \left[\int d^3 \mathbf{r} \rho(\mathbf{r}, t) V_{\text{en}}(\mathbf{r}, \{\mathbf{R}(t)\}) + \frac{1}{2} \sum_{I \neq J}^{N_{\text{ion}}} \frac{Z_I Z_J}{|\mathbf{R}_I(t) - \mathbf{R}_J(t)|} \right]. \quad (2)$$

The total density is defined as the sum of the spin-up and spin-down densities:

$$\rho(\mathbf{r}, t) = \sum_{\sigma=\uparrow, \downarrow} \sum_{j=1}^N |\psi_j(\mathbf{r}\sigma, t)|^2, \quad (3)$$

where σ runs over the two possible spin channels.

In these equations, M_I and Z_I are respectively the mass and charge of the I th nucleus. The KS effective potential consists of the Hartree potential V_H , the exchange-correlation (xc) potential V_{xc} , and the electron-nucleus potential V_{en} . The ionic motion is coupled to the electronic dynamics through the electronic density $\rho(\mathbf{r}, t)$ in Eq. (2). The electrons and nuclei must be evolved simultaneously.

B. Initial state for nonbare projectiles

When simulating bare-ion collisions, one normally chooses the laboratory rest frame in which initially the target is static and the projectile—a charged classical point particle—is simply given an initial velocity. If the projectile has active electrons, however, one must consider more carefully the problem of preparing the initial state and the reference frame. To discuss this issue, we start first by considering the general problem of changing the reference frame for collision problems within the TDDFT formalism.

At the initial time, the active electrons consist of two spatially separated KS systems belonging to the target and projectile. Then, the following two steps are required: (1) One must prepare an initial state for both, which implies providing an initial velocity to both electrons and nuclei of the projectile—and perhaps also of the target, if we consider a reference frame in which the target is also not initially at rest. (2) All active electronic orbitals of both target and projectile systems are then propagated on the same footing, along with the ions, according to Eqs. (1) and (2). To prepare an electronic system with an initial velocity, one must consider how to transform the KS equations between reference frames.

Let us consider the problem in full generality: consider a KS system from the viewpoint of an accelerated observer whose position relative to the original reference frame is given by a transformed vector $\mathbf{x}(t)$. Also, we assume that the accelerated and original reference systems are both initially in their ground state, and the initial condition $\mathbf{x}(t_0) = 0$, so that the two reference systems initially coincide at t_0 . The accelerated observer can describe the time-dependent evolution of the system by the following transformed TDKS equations [25,42]:

$$i \frac{\partial}{\partial t} \psi_j^{\text{ob}}(\mathbf{r}\sigma, t) = \left[-\frac{1}{2} \nabla^2 + V_{\text{nc}}(\mathbf{r} + \mathbf{x}) + V_H(\mathbf{r} + \mathbf{x}, t) + V_{\text{xc}}(\mathbf{r} + \mathbf{x}, t) - \frac{\dot{\mathbf{x}}^2}{2} + \dot{\mathbf{x}} \cdot \mathbf{r} \right] \psi_j^{\text{ob}}(\mathbf{r}\sigma, t),$$

$$j = 1, 2, \dots, N. \quad (4)$$

The KSOs in the accelerated reference frame, ψ_j^{ob} , are related to the original ones by

$$\psi_j^{\text{ob}}(\mathbf{r}\sigma, t) = e^{-i\dot{\mathbf{x}} \cdot \mathbf{r}} \psi_j((\mathbf{r} + \mathbf{x})\sigma, t), \quad (5)$$

where we use the superscript “ob” to label the orbitals from the viewpoint of the observer. The modified KSOs are simply the product of the displaced original KSOs with a boosting phase factor $e^{-i\dot{\mathbf{x}} \cdot \mathbf{r}}$.

It is worth mentioning that the boosting phase factor used in this work is physically equivalent to the electron translation factor (ETF) [43], which has been widely implemented within close-coupling treatments [44] such as two-center atomic

expansions [45–47]. At infinite separation, the factor makes a single-electron wave function carry an additional linear momentum as well as a kinetic energy, avoiding nontravelling stationary states.

The resulting total density is given by

$$\rho^{\text{ob}}(\mathbf{r}, t) = \rho(\mathbf{r} + \mathbf{x}, t), \quad (6)$$

which illustrates that the result of the change of reference frame on the total density distribution is merely a coordinate displacement \mathbf{x} . At time zero, this displacement is zero, and the two densities coincide. It is also worth considering the transformation on the classical velocity of the density distribution, i.e., the velocity of the center of mass:

$$\mathbf{D}_c = \frac{1}{\int \rho(\mathbf{r}, t) d\mathbf{r}} \int \mathbf{r} \cdot \rho(\mathbf{r}, t) d\mathbf{r}. \quad (7)$$

Starting from Eq. (5), it is easy to prove that the transformed \mathbf{D}_c^{ob} satisfies

$$\mathbf{D}_c^{\text{ob}} = \mathbf{D}_c - \dot{\mathbf{x}}, \quad (8)$$

and the corresponding velocity is therefore given by

$$\mathbf{v}_c^{\text{ob}} = \frac{d\mathbf{D}_c^{\text{ob}}}{dt} = \frac{d(\mathbf{D}_c - \dot{\mathbf{x}})}{dt} = \mathbf{v}_c - \ddot{\mathbf{x}}. \quad (9)$$

The average velocity of the projectile system in the accelerated reference indeed relates to the original one by a velocity difference $-\ddot{\mathbf{x}}$ due to the relative motion.

The previous relations could be used to consider, for the problem at hand, the (accelerated) reference frames in which either the projectile, target, or center of mass, are constantly at rest. Depending on the particular problem, any choice for the reference frame can be computationally more advantageous. In this work, we simply consider an inertial frame in which one of the fragments has initial zero velocity, while the other does not. We do need the previous relations, however, in order to find what should be the initial KSOs of this latter fragment that has nonzero initial velocity (and is, therefore, the “projectile”). One starts by considering that, before the collision, this electronic system is initially in the ground state moving at a constant velocity \mathbf{u} . Therefore, in the reference frame in which its velocity is zero, the KSOs are the ground-state ones, $\psi_j^{\text{g.s.}}(\mathbf{r}\sigma, t)$. To transform these to the laboratory reference frame, one just needs to make use of Eq. (5), i.e., to “boost” the KSOs of the projectile system with the constant velocity \mathbf{u} : $\psi_j^{\text{g.s.}}(\mathbf{r}\sigma, t) \rightarrow e^{i\mathbf{u} \cdot \mathbf{r}} \psi_j^{\text{g.s.}}(\mathbf{r}\sigma, t)$.

Notice that the initial density remains invariant. Despite this fact, the transformation of the KSOs is crucial to yield results in quantitative accord with experimental data. It avoids an unphysical initial decoupling of the projectile nucleus and electrons.

C. Extraction of charge-transfer probability

The charge-transfer cross sections are defined in terms of the charge-transfer probabilities: if N_0^P and N_0^T are the initial number of electrons of the projectile and of the target, respectively, the probability of k -electron transfer from the projectile to the target is the probability of finding, at the end of the process, the target into any of the bound states with $N_0^T + k$ electrons. These may be written in terms of the overlap of the

final many-electron wave function onto these bound states, but the calculation of these is cumbersome, and unfeasible in the TDDFT formalism that we are using.

For this reason, we use a geometrical approximation based on the division of the real space into regions. The idea is to use projection operator techniques, in particular for the number operator and the associated projectors onto its eigensubspaces. The following description of this ‘‘particle number projector’’ (PNP) method is based on the results given in Refs. [33–36,48]. This technique has proven to be a powerful approach in many applications in nuclear physics [35,49–51]. For example, Simenel used the PNP method to investigate the sequential transfer of nucleons in heavy-ion collisions below the fusion barrier [34]. In the following, we make a brief summary of the method, considering only a two-region case: the electrons are either bound by the target or bound by the projectile (although see the discussion below on ionization), and ignoring the possibility of multifragmentation processes.

Consider a region τ of the full space. The hypothetical measurement of the number of electrons contained in that region is associated with the number operator observable for that region, that can be written in various equivalent ways:

$$\begin{aligned}\hat{N}_\tau &= \sum_\sigma \int_\tau d^3r \hat{\psi}_\sigma^\dagger(\mathbf{r}) \hat{\psi}_\sigma(\mathbf{r}) = \int_\tau d^3r \hat{n}(\mathbf{r}) \\ &= \int_\tau d^3r \sum_{i=1}^N \delta(\mathbf{r} - \hat{\mathbf{r}}_i) = \sum_{i=1}^N \int d^3r \Theta_\tau(\mathbf{r}) \delta(\mathbf{r} - \hat{\mathbf{r}}_i) \\ &= \sum_{i=1}^N \Theta_\tau(\hat{\mathbf{r}}_i).\end{aligned}\quad (10)$$

Here, $\hat{\psi}_\sigma^\dagger(\mathbf{r})$ and $\hat{\psi}_\sigma(\mathbf{r})$ are the creation and annihilation field operators, respectively, for one electron at position \mathbf{r} and with spin σ ; $\hat{n}(\mathbf{r}) = \sum_{i=1}^N \delta(\mathbf{r} - \hat{\mathbf{r}}_i)$ is the density operator, and Θ_τ is the characteristic function of τ :

$$\Theta_\tau(\mathbf{r}) = \begin{cases} 1 & \text{for } \mathbf{r} \in \tau \\ 0 & \text{for } \mathbf{r} \notin \tau. \end{cases}\quad (11)$$

The total number operator \hat{N} results from the integration of the density operator over all space, $\hat{N} = \int d^3r \hat{n}(\mathbf{r})$. Obviously, $\hat{N} = \hat{N}_\tau + \hat{N}_{\bar{\tau}}$, where $\bar{\tau}$ is the complement of τ .

The possible measurements of \hat{N}_τ (i.e., its eigenvalues) must be integer numbers, $n = 0, 1, \dots, N$. The probability of measuring n when the system is in state Ψ must be given by the projection of Ψ onto the subspace of eigenvectors of \hat{N}_τ associated with n . We call \hat{P}_n the corresponding projection operator, and P_n the associated probabilities:

$$P_n = \|\hat{P}_n|\Psi\rangle\|^2 = \langle\Psi|\hat{P}_n|\Psi\rangle.\quad (12)$$

The projectors \hat{P}_n can be written in several different manners. For example, consider first the set S of all possible sequences $(\boldsymbol{\tau}) = (\tau_1, \dots, \tau_N)$, where τ_i is either τ or its complement $\bar{\tau}$ (there are 2^N possible sequences in S). We then consider the subset $S_n \subset S$ of all of those sequences where τ appears n times and $\bar{\tau}$ appears $N - n$ times [there are $\binom{N}{n}$ sequences in S_n]. Using this definition, one may prove that

$$\hat{P}_n = \sum_{(\boldsymbol{\tau}) \in S_n} \Theta_{\tau_1}(\hat{\mathbf{r}}_1) \cdots \Theta_{\tau_N}(\hat{\mathbf{r}}_N).\quad (13)$$

Likewise, using projection operator techniques [36], one may also prove that, equivalently,

$$\hat{P}_n = \frac{1}{2\pi} \int_0^{2\pi} d\theta e^{i\theta(n - \hat{N}_\tau)}.\quad (14)$$

This expression, in fact, makes it easy to prove that \hat{P}_n is indeed the projector onto the eigensubspace of \hat{N}_τ associated with value n , i.e.,

$$\hat{N}_\tau \hat{P}_n = n \hat{P}_n.\quad (15)$$

The probabilities of finding n electrons when the system is in state Ψ [Eq. (12)] can now be written explicitly using these expressions for \hat{P}_n ; for example, using Eq. (13), one arrives at

$$P_n = \sum_{(\boldsymbol{\tau}) \in S_n} \int_{\tau_1} dx_1 \cdots \int_{\tau_N} dx_N |\Psi(x_1, \dots, x_N)|^2.\quad (16)$$

Here, we group the spatial and spin coordinates into the collective variable x_i and define $\sum_{\sigma_i} \int d^3r_i \equiv \int dx_i$. Using this formula and the normalization of Ψ , it is straightforward to check that $\sum_{n=0}^N P_n = 1$.

Up to now, all previous considerations are exact and general for any region τ . To apply these concepts to the collision processes, the idea is to define a region of space around, for example, the target ($\tau = V_T$) and identify the probability of finding n electrons bound to the target as the probability of finding n electrons in region V_T . This is a first approximation.

A second approximation that we will make is the substitution of the exact many-electron wave function Ψ by the one-determinant time-dependent Kohn-Sham fictitious wave function formed by one-electron orbitals ψ_1, \dots, ψ_N introduced above.

$$\Psi(x_1, \dots, x_N, t) = \frac{1}{\sqrt{N!}} \det\{\psi_i(x_j, t)\}.\quad (17)$$

Note that in DFT methods only the density of the Kohn-Sham system can be identified with that of the real one, and therefore this identification of the wave function is an approximation, whose validity is one of the issues at stake in this work.

In any case, if the wave function is, as we will assume hereafter, one Slater determinant, Eq. (16) can be substituted by

$$P_n = \sum_{(\boldsymbol{\tau}) \in S_n} \det\{\langle\psi_i|\psi_j\rangle_{\tau_i}\},\quad (18)$$

an equation that, to the best of our knowledge, was first provided by Ludde and Dreizler [33]. Here, we use an orbital overlap reduced to a given region, i.e.,

$$\langle\psi_i|\psi_j\rangle_X = \sum_\sigma \int_X d^3r \psi_i^*(\mathbf{r}\sigma) \psi_j(\mathbf{r}\sigma),\quad (19)$$

where X is either τ or its complement $\bar{\tau}$. Note that these objects satisfy the orthogonal relation:

$$\langle\psi_i|\psi_j\rangle_\tau = \delta_{ij} - \langle\psi_i|\psi_j\rangle_{\bar{\tau}},\quad (20)$$

and, therefore, the probability P_n can be computed by considering only one of the regions, and making use only of the inner products integrated in it, with no need of integrating or even knowing the value of the orbitals in the complementary region.

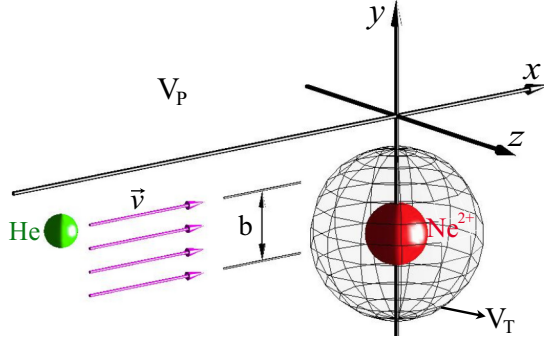


FIG. 1. The schematic diagram of the simulations, displaying the inverse collision framework. The He atom is treated as the projectile, and the Ne^{2+} ion as the target. The impact parameter is denoted by b , and pink arrows point out the incident direction. The whole space is divided into two, the region V_T that contains the target, and its complementary, the region V_P that contains the projectile.

There has been a few applications of Eq. (18) for many-electron systems [26,30,38,52]. However, it is computationally intensive due to the number of combinations contained in the set S : one has to deal with the determinant $\det\{\langle\psi_i|\psi_j\rangle_{\tau_i}\}$ for 2^N times to get the full series of charge-transfer probabilities P_n ($n = 0, 1, \dots, N$), which soon becomes prohibitive as N increases.

This can be alleviated, as suggested by Simenel [34], by departing, instead of from Eq. (13), from the expression (14) for \hat{P}_n . In that case, one arrives at

$$P_n = \frac{1}{2\pi} \int_0^{2\pi} d\theta \det(\langle\psi_i|\psi_j\rangle_{\bar{\tau}} + e^{-i\theta} \langle\psi_i|\psi_j\rangle_{\tau}). \quad (21)$$

In contrast with Eq. (18), the sum over a large number of determinants is substituted by an integral over the angles, and in this way the computation of the determinant $\det\{\langle\psi_i|\psi_j\rangle_{\tau_i}\}$ must be done ($N \times N_{\theta}$) times, with N_{θ} corresponding to the number of angles in the angular discretization. As a result, the use of Eq. (21) can indeed speed up the calculations, especially when one is dealing with systems with several tens of electrons. It is not difficult to demonstrate the fact that both methods are mathematically identical—see Ref. [35] for detailed derivations.

It only remains to relate the obtained probabilities with the energy-dependent cross section that k electrons transfer from the projectile to the target—the experimentally accessible magnitude. First, one must consider that the previously considered probabilities P_n are in fact function of E —the collision energy, i.e., the kinetic energy of the projectile—and of the impact parameter b (see Fig. 1): $P_n = P_n(E, b)$. Then, the cross sections can be computed by making use of the classical impact-parameter approximation, performing an integration over the impact parameter:

$$\sigma_k(E) = 2\pi \int_{b_{\min}}^{b_{\max}} db b P_{N_p^0 + k}(E, b), \quad (22)$$

where b is usually extended from an allowed minimum up to a sufficiently large value at which the target-projectile interaction is negligible.

D. Numerical details

1. Use of fractional occupation numbers

In this work, we concentrate on a Ne^{2+} ($3p$) ion colliding with a He ($1s$) atom at intermediate and high energies. To this end, we consider six active electrons for the Ne^{2+} ion ($2s^2 2p^4$) and two for the He atom ($1s^2$). Initially, both the atom and the ion are considered to be in their electronic ground states. The Ne^{2+} ion is, however, degenerate: in addition to two electrons occupying the $\psi_{2s\uparrow}$ and $\psi_{2s\downarrow}$ orbitals, there are four electrons that can occupy the six equal-energy orbitals $\{\psi_{2p_1\uparrow}, \psi_{2p_1\downarrow}, \psi_{2p_0\uparrow}, \psi_{2p_0\downarrow}, \psi_{2p_{-1}\uparrow}, \psi_{2p_{-1}\downarrow}\}$ [53].

Due to this degeneracy, the straightforward application of the theory presented in Sec. II C to the $\text{Ne}^{2+} + \text{He}$ collision would lead to spurious results because it was built on the assumption of a single nondegenerate ground state for both target and projectile. We must consider all possible degenerate initial states because they would all be present in the corresponding experiment. Fortunately, the ensemble-TDDFT [54] method provides a solution to this issue: Given the degeneracy, we must consider an ensemble of equally weighted and degenerate KS systems. These are described by single Slater determinants; in our case, to match up the PNP formalism, given that the total spin quantum number equals $S = 1$ and classified by the z -component spin $S_z = 1, 0, -1$, the following nine determinants are explicitly given for the fractionally occupied system [26]:

$$\begin{aligned} \Psi_{1,1} &= \det\{\psi_{1s\uparrow}\psi_{1s\downarrow}\psi_{2s\uparrow}\psi_{2s\downarrow}\psi_{2p_1\uparrow}\psi_{2p_1\downarrow}\psi_{2p_0\uparrow}\psi_{2p_{-1}\uparrow}\}, \\ \Psi_{2,1} &= \det\{\psi_{1s\uparrow}\psi_{1s\downarrow}\psi_{2s\uparrow}\psi_{2s\downarrow}\psi_{2p_1\uparrow}\psi_{2p_0\uparrow}\psi_{2p_0\downarrow}\psi_{2p_{-1}\uparrow}\}, \\ \Psi_{3,1} &= \det\{\psi_{1s\uparrow}\psi_{1s\downarrow}\psi_{2s\uparrow}\psi_{2s\downarrow}\psi_{2p_1\uparrow}\psi_{2p_0\uparrow}\psi_{2p_{-1}\uparrow}\psi_{2p_{-1}\downarrow}\}, \\ \Psi_{4,0} &= \frac{1}{\sqrt{2}}(\det\{\psi_{1s\uparrow}\psi_{1s\downarrow}\psi_{2s\uparrow}\psi_{2s\downarrow}\psi_{2p_1\uparrow}\psi_{2p_1\downarrow}\psi_{2p_0\uparrow}\psi_{2p_{-1}\downarrow} \\ &\quad + \det\{\psi_{1s\uparrow}\psi_{1s\downarrow}\psi_{2s\uparrow}\psi_{2s\downarrow}\psi_{2p_1\uparrow}\psi_{2p_1\downarrow}\psi_{2p_0\downarrow}\psi_{2p_{-1}\uparrow}\}), \\ \Psi_{5,0} &= \frac{1}{\sqrt{2}}(\det\{\psi_{1s\uparrow}\psi_{1s\downarrow}\psi_{2s\uparrow}\psi_{2s\downarrow}\psi_{2p_1\uparrow}\psi_{2p_0\uparrow}\psi_{2p_0\downarrow}\psi_{2p_{-1}\downarrow} \\ &\quad + \det\{\psi_{1s\uparrow}\psi_{1s\downarrow}\psi_{2s\uparrow}\psi_{2s\downarrow}\psi_{2p_1\downarrow}\psi_{2p_0\uparrow}\psi_{2p_0\downarrow}\psi_{2p_{-1}\uparrow}\}), \\ \Psi_{6,0} &= \frac{1}{\sqrt{2}}(\det\{\psi_{1s\uparrow}\psi_{1s\downarrow}\psi_{2s\uparrow}\psi_{2s\downarrow}\psi_{2p_1\uparrow}\psi_{2p_0\downarrow}\psi_{2p_{-1}\uparrow}\psi_{2p_{-1}\downarrow} \\ &\quad + \det\{\psi_{1s\uparrow}\psi_{1s\downarrow}\psi_{2s\uparrow}\psi_{2s\downarrow}\psi_{2p_1\downarrow}\psi_{2p_0\uparrow}\psi_{2p_{-1}\uparrow}\psi_{2p_{-1}\downarrow}\}), \\ \Psi_{7,-1} &= \det\{\psi_{1s\uparrow}\psi_{1s\downarrow}\psi_{2s\uparrow}\psi_{2s\downarrow}\psi_{2p_1\uparrow}\psi_{2p_1\downarrow}\psi_{2p_0\downarrow}\psi_{2p_{-1}\downarrow}\}, \\ \Psi_{8,-1} &= \det\{\psi_{1s\uparrow}\psi_{1s\downarrow}\psi_{2s\uparrow}\psi_{2s\downarrow}\psi_{2p_1\downarrow}\psi_{2p_0\uparrow}\psi_{2p_0\downarrow}\psi_{2p_{-1}\downarrow}\}, \\ \Psi_{9,-1} &= \det\{\psi_{1s\uparrow}\psi_{1s\downarrow}\psi_{2s\uparrow}\psi_{2s\downarrow}\psi_{2p_1\downarrow}\psi_{2p_0\downarrow}\psi_{2p_{-1}\uparrow}\psi_{2p_{-1}\downarrow}\}. \end{aligned}$$

Note that this labeling of the orbitals corresponds to the (initial) ground-state configuration; as soon as the collision happens, their s or p character is lost.

Within ensemble-TDDFT, one need not, however, make nine different propagations, one for each of the Slater determinants listed above. The procedure consists of propagating the TDKS equations for all the 10 KSOs, populating these orbitals with the eight electrons by making use of fractional occupation numbers: since the $2p^4$ electrons of Ne^{2+} ion must occupy six orbitals, a fractional occupation number of $2/3$ is thus assigned to each orbital in order to retain the symmetry of the $2p$ orbital, whereas the s electrons have an integer

occupation number of one. To compute the density of the ensemble, one must then substitute Eq. (3) by

$$\rho(\mathbf{r}, t) = \sum_{\sigma=\uparrow,\downarrow} \sum_{j=1}^{N_\sigma} f_j |\psi_j(\mathbf{r}\sigma, t)|^2, \quad (23)$$

where f_j are the occupation numbers. Summarizing, in our calculations, in order to describe the $\text{Ne}^{2+} + \text{He}$ collision, we have eight active electrons distributed over 10 KSOs.

The charge-transfer probability P_n is then calculated by averaging the probabilities of all configurations:

$$P_n = \sum_{i=1}^9 \omega_i P_n^i, \quad (24)$$

where P_n^i is the charge-transfer probability of configuration i . We assume the weight of every configuration to be $\omega_i = 1/9$, equal for all of them.

2. An inverse collision framework

All previous considerations assume that the calculations may follow the evolution of all KSOs during the full process. In our real-space numerical implementation of the theory, however, the KSOs and other variables must be enclosed in a finite but large (for convergence reasons) simulation box. We may initially enclose both projectile and target in this box, and therefore the starting KSOs are capable of describing the full electronic system at time zero. After the collision, however, the projectile abandons the simulation box, carrying part of the electrons with it, a fact that is handled by making use of absorbing boundary conditions, that deplete the part of each KSO that approaches the simulation box boundary. This is of course an approximation and introduces the error of assuming that the parts of the KSOs that remain in the simulation box evolve *as if* the full KSOs were propagated—when in fact the influence of the external fraction is being ignored.

The application of the PNP method must be done after the collision has taken place, and therefore the projectile has abandoned the simulation box—whereas the target remains in it. The region τ used for the application of the PNP method is therefore that of the target: a volume V_T around the target fragment that is contained in the simulation box, or is even coincident with the full simulation box. Its complement is V_P , although it should be clear that the electron charge contained in V_P is not necessarily bound to the projectile, as some ionization may take place, as we show below. Thanks to relation (20), one does not need to compute the overlaps in V_P —which is outside the simulation box anyways.

These considerations take us back to the problem of deciding on the reference frame: in essence, this amounts to deciding which ion to be considered as target, and which one as the projectile. From the viewpoint of the experimentalist, one would normally consider the He atom to be the target and Ne^{2+} to be the projectile—but as discussed in Sec. II B, one may change the reference frame and, with it, the apparent role of the ions. Physically, an inverse framework is, in principle, equivalent to the normal one, as long as one performs correctly the Galilean transformation [38,55]. Numerically, the choice

has consequences given the approximations mentioned above: the electrons around the projectile are ignored, and the results depend on the quality of the description of the electronic cloud around the target. In keV regimes, postcollision ionization of the nonbare Ne^{2+} usually lasts hundreds of femtoseconds, resulting in a sustained decreasing of the capture probabilities. To extract the probabilities as accurately as possible, it is necessary to set a long propagation time, and, more importantly, to obtain the electronic wave functions associated with the scattered Ne ion. We have found that, in this case, the inverse collision framework, in which Ne^{2+} is the target, is the most convenient choice. Therefore, we initially boost the He atom and then use it to impact the Ne^{2+} target. The reason is that this fragment contains most of the electrons of the system, and it is the one that gains electrons through charge transfer. After the collision, the Ne target and its associated electrons remain in the target region, V_T , whereas the ionized electrons and those bounded by the scattered He exist in the complementary region, V_P .

All calculations are carried out by the OCTOPUS program [56–58]. All numerical quantities are discretized in a rectangular box ($64 \times 34 \times 24a_0^3$) with a uniform grid spacing of $0.4a_0$. The simulation diagram is shown in Fig. 1. As it is shown there, the boosted He atom is initially positioned at $(-20a_0, -5a_0 + b, 0)$, where b is varied from 0.2 to $5a_0$ with $\Delta b = 0.2a_0$ and from 5 to $10a_0$ with $\Delta b = 0.25a_0$, and the ground-state Ne^{2+} ion is initially placed at $(0, -5a_0, 0)$. The initial velocity \vec{v} points along the positive x axis, and we vary its magnitude from the one corresponding to Ne^{2+} ions at 10 keV, to 3 MeV. The core electrons of Ne ion are frozen through the use of an optimized soft norm-conserving pseudopotential [59] that describes the core-electron effects. The adiabatic local density approximation (ALDA) [37] is employed as the xc functional. The equation for the nuclear motion is solved by the velocity Verlet algorithm [60]. With respect to the time evolution and the size of V_T , the total simulation time is set to 350 fs and the V_T covers the whole simulation box, which were found to be enough to ensure converged electron-capture cross sections (more numerical details can be found in the Appendix). The iteration time step is fixed to 4.83×10^{-4} fs. A complex absorbing potential (CAP) boundary [61] is used, with \sin^2 form and a width of $2a_0$ at each edge in all simulation boundaries.

III. RESULTS AND DISCUSSIONS

A. Single- and double-charge transfer cross sections

We present calculated single- and double-charge transfer cross sections as a function of impact energy in the range 10–3000 keV, where experimental data and other theoretical results are partially available, in Fig. 2. This impact energy is defined as the incident energy of the Ne^{2+} ion.

Regarding single-charge transfer (SCT) cross sections, shown in Fig. 2(a), on the whole, the present results agree fairly well with experiments: a maximum occurs at about 200 keV, beyond which the curve is seen to decay monotonically with the impact energy. Quantitatively, for energies larger than 200 keV, our results are consistent with those measured by Nikolaev *et al.* and Kase *et al.* to within an

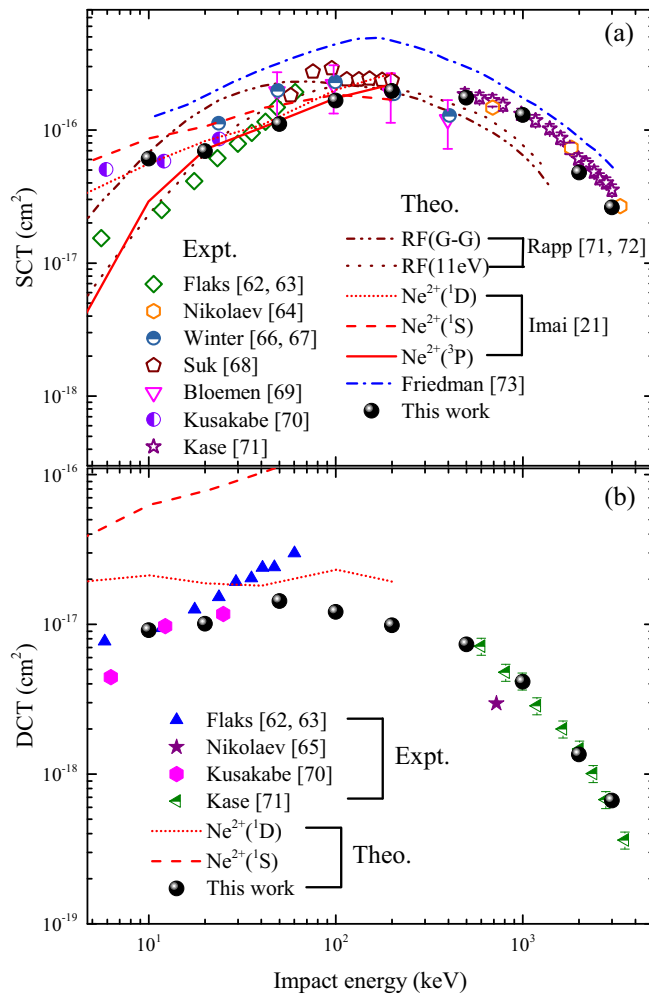


FIG. 2. Single- and double-charge transfer cross sections as a function of impact energy. The present results shown by full black circles are calculated by choosing the Ne^{2+} region (V_T) to be the whole simulation box. The other scattered symbols are experimental data of Flaks from Refs. [62,63], Nikolaev from Refs. [64,65], Winter from Refs. [66,67], Suk from Ref. [68], Bloemen from Ref. [69], Kusakabe from Ref. [70], and Kase from Ref. [71]. The curves are calculations from Rapp and Francis theory [71,72], the MOCC method calculations are from Ref. [21], and the results of Friedman are reported in Ref. [73].

accuracy of around 2%–18%, but overestimate the results from Winter *et al.* and Bloemen *et al.* by a factor of about two. For energies lower than 200 keV, our results do not match quantitatively the previous experiments, but the overall trend is similar. Surprisingly, the present data points are still within the error bars of the measurements of Bloemen *et al.* It should be noted, however, that there are substantial deviations among the various experiments: for example, the value reported by Kusakabe *et al.* is higher than that of Flaks *et al.* by about a factor of three at 10 keV. One of the main reasons might be attributed to the impurity of the Ne^{2+} ions in the experiments: a portion of the metastable ions brought in the ion beam of Ne^{2+} may lead to a fluctuation of the SCT cross sections. The possible treatment of this issue is beyond the scope of the present study.

Other theoretical results from semiclassical models either overestimate or underestimate experimental data, depending on the energy range. For example, Friedman *et al.* [73] recently proposed a semi-empirical scaling rule for SCT cross sections which overestimates the experimental results roughly by a factor of three. The calculated curves, which use an interpolating formula in terms of ionization potentials, deviate remarkably from experiments, especially at high impact energies. Rapp *et al.* [72] calculated the SCT cross sections considering the ground and excited states of the Ne^{2+} ion and are respectively plotted as RF(G-G) and RF(11eV) in Fig. 2(a). The discrepancy may indicate the fact that an inadequate description of the active electrons of Ne^{2+} can significantly influence charge-transfer process. Other calculations based on a molecular-orbital close-coupling (MOCC) method considered singlet and triplet states, i.e., $\text{Ne}^{2+}(^1D)$, $\text{Ne}^{2+}(^1S)$, and $\text{Ne}^{2+}(^3P)$, for collision energies below 200 keV. Our results are in good agreement with these MOCC calculations for the $\text{Ne}^{2+}(^3P)$ case, except at 10 keV, where our result happens to be in line with the $\text{Ne}^{2+}(^1D)$ result. Unfortunately, the absence of MOCC results at high energies prevents further comparison. The MOCC results cannot be extended beyond the maximum of the cross sections because the molecular expansion with a common ETF does not correctly separate electron-capture and target ionization [74]. Besides, the straight-line approximation is employed to describe projectile trajectory, but taking into account trajectory effects would lead to a decrease of the cross section since the transitions in the rectilinear trajectories take place at short internuclear separations that are not accessible for curved trajectories [75]. As a matter of fact, the MOCC study of Imai *et al.* [21] is considered to provide evidence that metastable ions can play a role in the measurement of ground-state ions. In summary, from all theoretical models, the TDDFT calculations not only reproduce more satisfactorily the SCT numbers but also are applicable to a more extended energy range.

The double-charge transfer (DCT) cross sections are shown in Fig. 2(b). It shows how these DCT cross sections are generally lower than the SCT cross sections by more than one order of magnitude. Double-charge transfer is a relatively weak process, and thereby it has been rarely investigated both experimentally and theoretically. The present DCT results are in excellent agreement with the experiments of Kase *et al.* at 500–3000 keV and are quantitatively comparable with the results of Kusakabe *et al.* at 10–20 keV. Early measurements from Flaks *et al.* show a monotonic growing trend with increasing the energy below 60 keV. It is hard to compare with the results of Nikolaev *et al.* since the authors merely measured the DCT at 600 keV. Regarding the MOCC calculations, it seems that the $\text{Ne}^{2+}(^1D)$ results are independent of impact energy, whereas the $\text{Ne}^{2+}(^1S)$ results show a rapid increasing curve, which considerably overestimates the experiments. To our knowledge, $\text{Ne}^{2+}(^3P)$ results are not available. Interestingly, the present TDDFT results smoothly connect the experiments from low to high energies. In particular, these results fill in the broad gap at the intermediate energies (60–500 keV), where experiments are absent for some reason. Future experiments would be desirable to confirm our predictions.

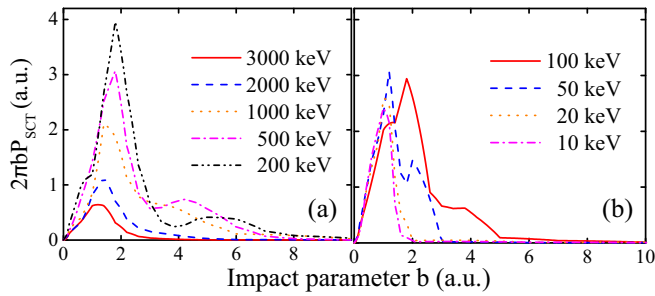


FIG. 3. Single-electron-capture probability as a function of impact parameter for impact energies at (a) 200–3000 keV and (b) 10–100 keV.

B. Electron-capture probabilities

Although we have found a good agreement for charge-transfer cross sections between the present TDDFT calculations and experiments in the preceding section, it can be also useful to examine the more detailed electron-capture probabilities from which the cross sections are calculated. In this way, we can learn about the dependence on the impact parameter and collision energy. To this end, we plot the calculated probability $2\pi bP$ as a function of impact parameter in Figs. 3 and 4 for a sequence of energies for single and double electron capture, respectively. It should be noted that electron capture of more than two electrons is impossible, as the source of the electrons, He, has only two electrons.

Single-electron-capture processes, shown in Fig. 3, have a unimodal distribution peaked at $1.5a_0$ and $1.2a_0$ at 2000 and 3000 keV, respectively. As the energy is decreased to 1000 keV, the peak magnitude and its width are enhanced, while a feature starts to grow in the region of moderate impact parameters ($b = 3a_0$ – $6a_0$). At 500 keV, we observe a bimodal distribution peaked at $b \approx 2$ and $4.2a_0$. A similar bimodal curve is also seen at 200 keV, but with a steady broad structure extended around $5.6a_0$. The position of the second peak is then shifted to $3.9a_0$ at 100 keV. Interestingly, the unimodal structure appears again at low energies (10 and 20 keV). All in all, the probability distribution can be categorized as “bimodal” for the intermediate-energy region, and as “unimodal” in other regions. At low energies, the projectile interacts with the target for much longer time than at high energies, although its interaction is limited by the available energy that can be deposited into the target. In contrast, at high-energies the projectile ion suffers from much too short an interaction time, even below

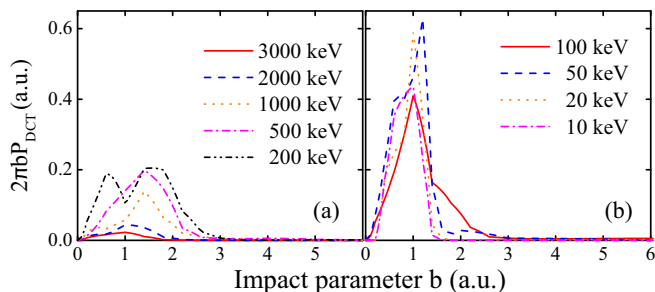


FIG. 4. Same as Fig. 3, but for double-electron-capture probability.

one femtosecond. The situation is slightly different for the intermediate-energy region, where the projectile is capable of capturing the electron in a wide b range. The enhancement in the cross sections may be interpreted as a velocity-matching effect, e.g., for $\text{Ne}^{2+}({}^3P)$ the energy region of 200–500 keV corresponds to a velocity of 0.63–1.00 a.u., which is close to that of $1s$ electrons in the neutral He atom. Previous studies have reported that electronic states and their angular orientations may significantly affect the charge-transfer processes near the velocity-matching region [76,77].

Figure 4 presents double-electron-capture probabilities. As expected, the magnitudes of DCT probabilities are much lower than those of SCT, by more than one order of magnitude—especially for the intermediate- and high-energy regions. The unimodal distribution is observed for all the selected energies, except for 200 keV, for which two peaks are located nearly symmetrically around $b = 1a_0$. However, we notice that the dependence of the peak location with respect to the energy is similar to that shown in Fig. 3 for the single-electron case. Here, the probability curve corresponding to 50 keV yields the largest DCT cross section. DCT processes seem to be dominated by close collisions ($b \leq 3a_0$), while SCT processes can take place for a wider range of impact parameters.

The impact-parameter effects can be further interpreted by making use of the potential-energy curves (PECs). Using a configuration-interaction (CI) method, Mercier *et al.* [78] calculated the diabatic PECs of NeHe^{2+} for the ground state, and for some low-lying excited states. Basically, they found a series of crossings among these states at short internuclear distances (less than $3a_0$). The DCT process was suggested to be an intermediary for electron capture to the excited $\text{Ne}^+({}^2S)$ states. Consistent with the existence of these crossings, our results predominantly present a short-range distance feature for both SCT and DCT probabilities in the region of $0a_0$ – $3a_0$.

C. Electron loss process

In ion-atom collisions, there are three main outcome channels [79]: electron capture (transfer), excitation, and ionization. Each one of these may be dominant, depending on the collision energy. Regarding ionization, the electron ejection can proceed through a one-step or a multiple-step process [80]. The former is also called direct ionization: electrons are promoted directly from bound to continuum states. The latter process consists of a series of transitions to intermediate states, which finish with a final transition to the continuum. In this section, we focus on the analysis of the electron loss during the $\text{Ne}^{2+} + \text{He}$ collision, showing how it influences the charge-transfer probabilities, and hence the cross sections.

For this purpose, we have analyzed the time-resolved values of electron-capture probabilities. In the previous sections, we have displayed values for these probabilities (and the corresponding cross sections) computed at very long times, when the process has reached convergence with respect to the propagation time. Before those converged values are achieved, however, the probabilities are depleted as a function of time, as part of the electronic charge abandons the target region. Long after the projectile has passed, that depletion can only be assigned to ionization.

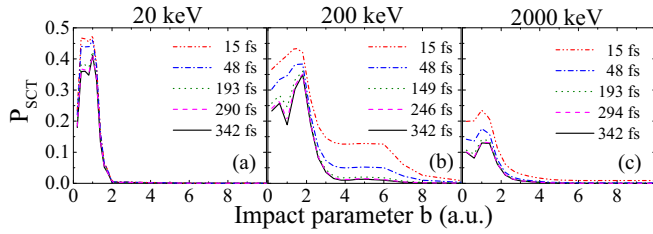


FIG. 5. The SCT probability as a function of impact parameter and simulation time at 20, 200, and 2000 keV. The entire numerical box is considered to be the Ne^{2+} target region V_T .

Therefore, we will now show the electron-capture probabilities as they vary in time before the convergence is achieved. The single-electron-capture probabilities (for 20, 200, and 2000 keV collisions) are displayed as a function of time in Fig. 5. As can be seen, the electron capture is stabilized after 200 fs. Before that, the region of the peak plateau shrinks considerably as time passes. This attenuation of the SCT probability until convergence is due to the slow transition to the continuum, i.e., a postcollision ionization of the Ne ion. The shapes of the curves corresponding to the 20 and 2000 keV energies do not change with time. However, at the intermediate energies (200 keV), the subsequent ionization does not only lower the electron-capture probability, but also modifies the peak structures: the peak at about $1a_0$ is gradually split up into two independent peaks, and, interestingly, the plateau-like region for $b \approx 3a_0 - 6a_0$ is suppressed by nearly one order of magnitude. A similar behavior was also observed for the double electron processes.

To further illustrate this ionization process, Fig. 6 shows the electronic density distribution inside the simulation box, for 200 keV collisions, for the sequence of time instants also displayed in Fig. 5(b). It should be mentioned here that the Ne^{2+} , at those times, is almost isolated from the He atom, due to their long separation. The electronic density distributions become more localized as the time increases. The ionized electrons are gradually absorbed by the boundaries, and the remaining electrons get more concentrated around the Ne ion. We display the processes for three different impact parameters b , since this plays a key role in the ionization process. At $b = 0.2a_0$, the Ne nucleus suffers an obvious displacement on the $+X$ axis, and the electronic density is highly dispersed throughout the simulation box. This is an obvious case of close collision, in which a lot of the impact energy is transferred to the nuclear kinetic energy and to the electronic excited states. In the lower panels, as b is increased to $3a_0$ and $6a_0$, the nuclear motion becomes less obvious, and the electronic excitation is weaker.

A number of experiments [69,80–82] have also reported the formation of ionizing states of multiply charged Ne ions in collisions with noble gases (e.g., He, Ar, Xe) at keV energies. A more detailed study of these electronic states is unfortunately not possible within TDDFT, and it would require more elaborate wave-function methods.

Finally, we display in Fig. 7 the “cross section decay,” which we define as the difference of the electron-capture cross section computed at time t and the one computed at a final converged t_∞ (in practice, we have found this convergence

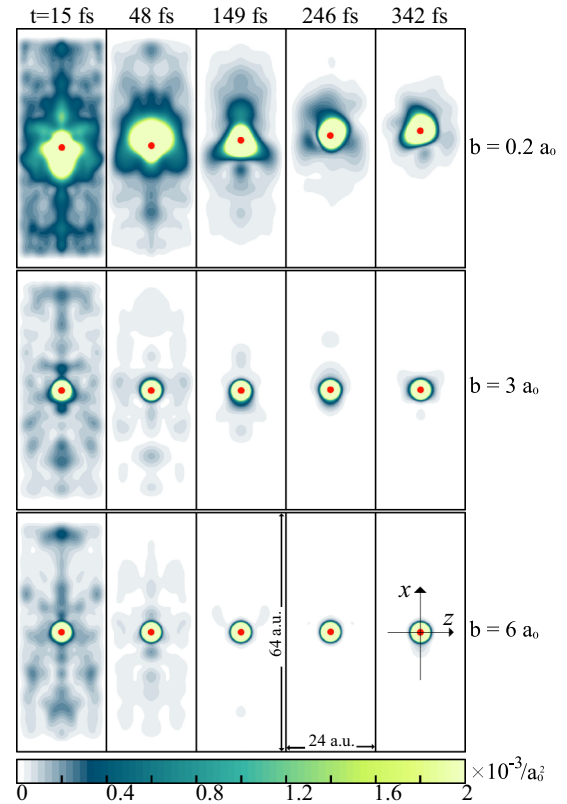


FIG. 6. Snapshots of the electronic density distribution inside the simulation box for 200 keV collisions, for the sequence of time instants displayed in Fig. 5(b). (top panel) $b = 0.2a_0$, (middle panel) $b = 3a_0$, (bottom panel) $b = 6a_0$. The red dot represents the Ne nucleus. The density values are represented by the colors mapped in the color bar.

t_∞ at around 350 fs). For example, for the SCT process at 200 and 2000 keV, the cross sections at 15 fs are about triple and double, respectively, than the converged cross sections shown in Fig. 2. For the 20 keV collision, however, although the value at 15 fs is still higher than the converged one, it is already comparable. It is evident that the decaying rate strongly depends on the impact energy. For example, it rapidly converges within about 75 fs for the 2000 keV collision, whereas it requires more than 200 fs for the 200 keV one. Basically, the same patterns can also be found for the DCT processes, perhaps even more pronounced.

IV. CONCLUSIONS

We have theoretically studied the SCT and DCT processes for the $\text{Ne}^{2+} + \text{He}$ collision, using the TDDFT-Ehrenfest formalism. To account for the initial velocity of the active electrons of the projectile, they are initially boosted with a phase transformation. The KSOs are then propagated in an inverse collision framework for a long time (typically several hundreds of fs), which guarantees that the scattering wave functions are fully converged. At a sufficiently long final time, the charge-transfer probabilities are extracted by making use of a particle number projection technique. Due to the ground-state degeneracy of the initial state, we employ an

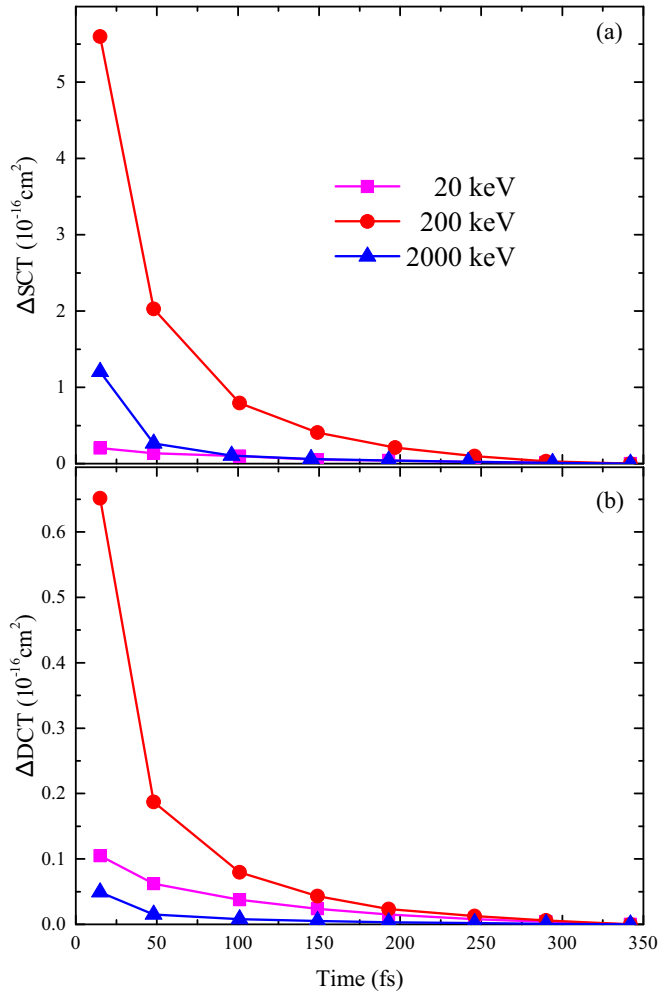


FIG. 7. The increment of (a) SCT and (b) DCT cross sections calculated at the time instant t relative to the converged ones, e.g., $\Delta\sigma_{\text{SCT(DCT)}} = \sigma_{\text{SCT(DCT)}}(t) - \sigma_{\text{SCT(DCT)}}(t \rightarrow \infty)$. The solid curves are shown to guide the eye.

ensemble-TDDFT formulation that requires fractional occupation numbers for the orbitals.

Our calculated single- and double-charge transfer cross sections show good agreement with experiments. For the DCT process, we provide results at intermediate energies (60–500 keV), for which no measured data exist. Quantitatively, our results outperform other theoretical calculations for $\text{Ne}^{2+} + \text{He}$ collisions. By analyzing the impact-parameter-dependent charge-transfer probabilities, we have found that these peak in the region below $3a_0$. Finally, a time-resolved analysis has provided a quantitative evaluation of the impact of electron loss on the charge-transfer cross sections. We conclude that this TDDFT-Ehrenfest formalism, in combination with the particle number projection technique, may provide satisfactory results for charge-transfer processes in ion-atom collisions.

Due to the good scalability of TDDFT, we expect that the present method will prove helpful to explore more complicated nonbare ion collisions, such as ions colliding with molecules or materials. For instance, one may be interested in the charge-transfer dynamics of biomolecules, or in the

stopping powers of solids. Another noteworthy possibility is the extension of the method to deal with excited or negatively charged projectiles colliding with periodic systems, which have been traditionally described by model potentials.

ACKNOWLEDGMENTS

We thank the referees for their valuable comments. This work was financially supported by the National Science Foundation of China under Contracts No. U1832201, No. 11704039, No. 11774030, No. 11704037, No. 11674067, No. 11534011, and No. 11404065, the European Research Council (ERC-2015-AdG694097), the Cluster of Excellence “Advanced Imaging of Matter” (AIM), Grupos Consolidados (IT1249-19) and SFB925 “Light induced dynamics and control of correlated quantum systems.” A.C. acknowledges financial support by MINECO Grant FIS2017-82426-P. The work of the second author (C.-Z.G.) was performed under the auspices of the China Academy of Engineering Physics (CAEP) Foundation (Grant No. PY20200142). The Flatiron Institute is a division of the Simons Foundation.

APPENDIX: CONVERGENCE WITH RESPECT TO THE TARGET REGION SIZE

In the present scheme, one crucial choice to make is the target region V_T , since it plays a decisive role in the equations that define the probability P_n . From these equations, it is clear that the cross sections in principle depend on the size of V_T . For this reason, we dedicate this Appendix to show how the final cross sections must be carefully checked for convergence with respect to the size of this region. The size must be large enough so that the final scattering states are fully contained in it. However, it cannot be too large because it would make the calculations unfeasible and also because excessively large regions would include electronic charge corresponding to ionized states.

In Table I we display cross-section values for various times and for three choices of the target region size. This region

TABLE I. The calculated SCT cross sections at 1000 keV for selected times (second column). The comparison is made among a variety of sizes for the Ne^{2+} region (first column). The benchmark value is $\sigma_{\text{SCT}} = (1.32 \pm 0.13) \times 10^{-16} \text{ cm}^2$.

$R_{V_T} (a_0)$	t (fs)	SCT cross section (10^{-16} cm^2)
Whole box ^a	48	2.16
	101	1.60
	197	1.38
	290	1.29
15	48	1.62
	101	1.40
	197	1.29
	290	1.24
5	48	0.91
	101	0.92
	197	0.93
	290	0.97

^aThe V_T region is the full simulation box.

is defined as a sphere of radius R_{V_T} centered on the Ne ion, although it is to be noted that, since the simulation box is a parallelepiped, V_T is in fact the intersection region of the full simulation box and that sphere.

For $R_{V_T} = 5a_0$, the calculated SCT cross sections are almost stable at all times, around $0.93 \times 10^{-16} \text{ cm}^2$, which is lower than the measured value, $\sigma_{\text{SCT}} = (1.32 \pm 0.13) \times 10^{-16} \text{ cm}^2$. The difference must be interpreted by the incomplete description of the final-time scattering states.

By increasing R_{V_T} , one obtains larger SCT results. For $R_{V_T} = 15a_0$, we see that the SCT results converge to an asymptotic value of 1.24, which already compares well with experiments, within the error bar. However, by still increasing R_{V_T} further, the cross section still changes slightly and saturates to its final value 1.29. In the main text, all the reported results are computed using the whole simulation box as V_T region. The chosen size for the simulation box was found to be big enough to obtain converged results.

-
- [1] F. Aumayr, K. Ueda, E. Sokell, S. Schippers, H. Sadeghpour, F. Merkt, T. F. Gallagher, F. B. Dunning, P. Scheier, O. Echt *et al.*, *J. Phys. B: At., Mol. Opt. Phys.* **52**, 171003 (2019).
- [2] C. Covington, K. Hartig, A. Russakoff, R. Kulpins, and K. Varga, *Phys. Rev. A* **95**, 052701 (2017).
- [3] T. Kirchner, L. Gulyás, H. J. Lüdde, A. Henne, E. Engel, and R. M. Dreizler, *Phys. Rev. Lett.* **79**, 1658 (1997).
- [4] H. Gilbody, *Phys. Scr.* **23**, 143 (1981).
- [5] R. K. Janev and L. Presnyakov, *Phys. Rep.* **70**, 1 (1981).
- [6] T. Kusakabe, Y. Miyamoto, R. Ishida, K. Itoh, N. Kuroyanagi, Y. Nakai, and T. Shirai, *Nucl. Instrum. Methods Phys. Res., Sect. B* **205**, 600 (2003).
- [7] J. Gallagher, B. Bransden, and R. Janev, *J. Phys. Chem. Ref. Data* **12**, 873 (1983).
- [8] W. Eckstein, in *Atomic and Plasma-Material Interaction Data for Fusion* (1991), Vol. 1, p. 51.
- [9] B. G. Lindsay and R. F. Stebbings, *J. Geophys. Res.: Space Phys.* **110**, A12213 (2005).
- [10] R. Dörner, V. Mergel, R. Ali, U. Buck, C. L. Cocke, K. Froschauer, O. Jagutzki, S. Lencinas, W. E. Meyerhof, S. Nüttgens, R. E. Olson, H. Schmidt-Bocking, L. Spielberger, K. Tokési, J. Ullrich, M. Unverzagt, and W. Wu, *Phys. Rev. Lett.* **72**, 3166 (1994).
- [11] R. E. Olson and A. Salop, *Phys. Rev. A* **16**, 531 (1977).
- [12] M. McDowell and R. Janev, *J. Phys. B: At. Mol. Phys.* **18**, L295 (1985).
- [13] G. Maynard, R. Janev, and K. Katsonis, *J. Phys. B: At., Mol. Opt. Phys.* **25**, 437 (1992).
- [14] O. J. Kroneisen, H. J. Lüdde, T. Kirchner, and R. M. Dreizler, *J. Phys. A: Math. Gen.* **32**, 2141 (1999).
- [15] T. Kirchner, A. C. F. Santos, H. Luna, M. M. Sant' Anna, W. S. Melo, G. M. Sigaud, and E. C. Montenegro, *Phys. Rev. A* **72**, 012707 (2005).
- [16] T. Kirchner and M. Horbatsch, *Phys. Rev. A* **63**, 062718 (2001).
- [17] T. Kirchner, M. Horbatsch, and H. Lüdde, *J. Phys. B: At., Mol. Opt. Phys.* **37**, 2379 (2004).
- [18] G. Schenk and T. Kirchner, *Phys. Rev. A* **91**, 052712 (2015).
- [19] T. Kirchner, M. Murakami, M. Horbatsch, and H. Lüdde, *J. Phys.: Conf. Ser.* **388**, 012038, (2012).
- [20] M. Baxter, T. Kirchner, and E. Engel, *Phys. Rev. A* **96**, 032708 (2017).
- [21] T. W. Imai, M. Kimura, J. P. Gu, G. Hirsch, R. J. Buenker, J. G. Wang, P. C. Stancil, and L. Pichl, *Phys. Rev. A* **68**, 012716 (2003).
- [22] J. K. M. Eichler, A. Tsuji, and T. Ishihara, *Phys. Rev. A* **23**, 2833 (1981).
- [23] L. Gulyás, P. D. Fainstein, and T. Shirai, *Phys. Rev. A* **65**, 052720 (2002).
- [24] E. Runge and E. K. U. Gross, *Phys. Rev. Lett.* **52**, 997 (1984).
- [25] C. Ullrich, *Time-Dependent Density-Functional Theory: Concepts and Applications* (Oxford University Press, 2012).
- [26] F. Wang, X. Hong, J. Wang, and K. S. Kim, *J. Chem. Phys.* **134**, 154308 (2011).
- [27] A. Castro, M. Isla, J. I. Martínez, and J. A. Alonso, *Chem. Phys.* **399**, 130 (2012).
- [28] S. Bubin, B. Wang, S. Pantelides, and K. Varga, *Phys. Rev. B* **85**, 235435 (2012).
- [29] C.-Z. Gao, J. Wang, F. Wang, and F.-S. Zhang, *J. Chem. Phys.* **140**, 054308 (2014).
- [30] X. Hong, F. Wang, Y. Wu, B. Gou, and J. Wang, *Phys. Rev. A* **93**, 062706 (2016).
- [31] G. Bi, J. Kang, and L.-W. Wang, *Phys. Chem. Chem. Phys.* **19**, 9053 (2017).
- [32] R. Ullah, E. Artacho, and A. A. Correa, *Phys. Rev. Lett.* **121**, 116401 (2018).
- [33] H. Ludde and R. Dreizler, *J. Phys. B: At. Mol. Phys.* **16**, 3973 (1983).
- [34] C. Simenel, *Phys. Rev. Lett.* **105**, 192701 (2010).
- [35] K. Sekizawa and K. Yabana, *Phys. Rev. C* **88**, 014614 (2013).
- [36] M. Bender, P.-H. Heenen, and P.-G. Reinhard, *Rev. Mod. Phys.* **75**, 121 (2003).
- [37] J. P. Perdew, *Phys. Rev. B* **33**, 8822 (1986).
- [38] R. Nagano, K. Yabana, T. Tazawa, and Y. Abe, *Phys. Rev. A* **62**, 062721 (2000).
- [39] E. E. Quashie, B. C. Saha, X. Andrade, and A. A. Correa, *Phys. Rev. A* **95**, 042517 (2017).
- [40] O. A. Vydrov and G. E. Scuseria, *J. Chem. Phys.* **122**, 184107 (2005).
- [41] F. Calvayrac, P.-G. Reinhard, E. Suraud, and C. Ullrich, *Phys. Rep.* **337**, 493 (2000).
- [42] G. Vignale, *Phys. Rev. Lett.* **74**, 3233 (1995).
- [43] D. R. Bates and R. McCarroll, *Proc. R. Soc. London, Ser. A* **245**, 175 (1958).
- [44] W. Fritsch and C. D. Lin, *Phys. Rep.* **202**, 1 (1991).
- [45] M. Zapukhlyak, T. Kirchner, H. Lüdde, S. Knoop, R. Morgenstern, and R. Hoekstra, *J. Phys. B: At., Mol. Opt. Phys.* **38**, 2353 (2005).
- [46] J. W. Gao, Y. Wu, J. G. Wang, N. Sisourat, and A. Dubois, *Phys. Rev. A* **97**, 052709 (2018).
- [47] J. W. Gao, Y. Wu, J. G. Wang, A. Dubois, and N. Sisourat, *Phys. Rev. Lett.* **122**, 093402 (2019).
- [48] H. Ludde and R. Dreizler, *J. Phys. B: At. Mol. Phys.* **18**, 107 (1985).

- [49] J. Dobaczewski, M. V. Stoitsov, W. Nazarewicz, and P.-G. Reinhard, *Phys. Rev. C* **76**, 054315 (2007).
- [50] M. Samyn, S. Goriely, M. Bender, and J. M. Pearson, *Phys. Rev. C* **70**, 044309 (2004).
- [51] K. Sekizawa and K. Yabana, *Phys. Rev. C* **93**, 029902(E) (2016).
- [52] R. Nagano, K. Yabana, T. Tazawa, and Y. Abe, *J. Phys. B: At., Mol. Opt. Phys.* **32**, L65 (1999).
- [53] For p orbitals, the relationship between real orbitals in Cartesian coordinates and complex orbitals in spherical coordinates is $p_x = 1/\sqrt{2}(p_1 + p_{-1})$, $p_y = 1/(i\sqrt{2})(p_1 - p_{-1})$, and $p_z = p_0$, where $p_m = R_n Y_{lm}$ with $m = 0, \pm 1$ and n identical to principal quantum number. By definition, complex orbitals are the product of the radial function R and the spherical harmonics Y .
- [54] T. Li and Y. Li, *Phys. Rev. A* **31**, 3970 (1985).
- [55] C. Illescas, M. Lombana, L. Méndez, I. Rabadán, and J. Suárez, *Phys. Chem. Chem. Phys.* **22**, 19573 (2020).
- [56] M. A. Marques, A. Castro, G. F. Bertsch, and A. Rubio, *Comput. Phys. Commun.* **151**, 60 (2003).
- [57] A. Castro, H. Appel, M. Oliveira, C. A. Rozzi, X. Andrade, F. Lorenzen, M. A. Marques, E. Gross, and A. Rubio, *Phys. Status Solidi B* **243**, 2465 (2006).
- [58] N. Tancogne-Dejean, M. J. Oliveira, X. Andrade, H. Appel, C. H. Borca, G. Le Breton, F. Buchholz, A. Castro, S. Corni, A. A. Correa *et al.*, *J. Chem. Phys.* **152**, 124119 (2020).
- [59] M. Schlipf and F. Gygi, *Comput. Phys. Commun.* **196**, 36 (2015).
- [60] A. Gómez Pueyo, M. A. Marques, A. Rubio, and A. Castro, *J. Chem. Theory Comput.* **14**, 3040 (2018).
- [61] D. E. Manolopoulos, *J. Chem. Phys.* **117**, 9552 (2002).
- [62] I. Flaks and E. Solovev, *Sou. Phys.-Tech. Phys.* **3**, 564 (1958).
- [63] I. Flaks and E. Solovev, *Sou. Phys.-Tech. Phys.* **3**, 577 (1958).
- [64] V. S. Nikolaev, I. S. Dmitriev, L. N. Fateeva, and Ya. A. Teplova, *Sov. Phys. JETP* **13**, 695 (1961).
- [65] V. Nikolaev, L. Fateeva, S. DMITRIEV, and Y. A. Teplova, *Sov. Phys. JETP* **14**, 67 (1962).
- [66] H. Winter, E. Bloemen, and F. der Heer, *J. Phys. B: At. Mol. Phys.* **10**, L453 (1977).
- [67] H. Winter, E. Bleomen, and F. De Heer, *J. Phys. B: At. Mol. Phys.* **10**, L599 (1977).
- [68] H. Suk, A. Guilbaud, and B. Hird, *J. Phys. B: At. Mol. Phys.* **11**, 1463 (1978).
- [69] E. Bloemen, D. Dijkkamp, and F. de Heer, *J. Phys. B: At. Mol. Phys.* **15**, 1391 (1982).
- [70] T. Kusakabe, N. Nagai, H. Hanaki, T. Horiuchi, and M. Sakisaka, *J. Phys. Soc. Jpn.* **52**, 4122 (1983).
- [71] M. Kase, A. Kikuchi, A. Yagishita, and Y. Nakai, *J. Phys. B: At. Mol. Phys.* **17**, 671 (1984).
- [72] D. Rapp and W. E. Francis, *J. Chem. Phys.* **37**, 2631 (1962).
- [73] B. Friedman and G. DuCharme, *J. Phys. B: At., Mol. Opt. Phys.* **50**, 115202 (2017).
- [74] L. Errea, C. Harel, H. Jouini, L. Méndez, B. Pons, and A. Riera, *J. Phys. B: At., Mol. Opt. Phys.* **27**, 3603 (1994).
- [75] L. F. Errea, F. Guzmán, L. Méndez, B. Pons, and A. Riera, *Phys. Rev. A* **77**, 012706 (2008).
- [76] K. B. MacAdam, R. Rolfes, and D. A. Crosby, *Phys. Rev. A* **24**, 1286 (1981).
- [77] E. Y. Sidky and H.-J. T. Simonsen, *Phys. Rev. A* **54**, 1417 (1996).
- [78] E. Mercier, G. Chambaud, and B. Levy, *J. Phys. B: At. Mol. Phys.* **18**, 3591 (1985).
- [79] D. Belkić, *Adv. At. Mol. Opt. Phys.* **56**, 251 (2009).
- [80] D. Vernhet, L. Adoui, J. P. Rozet, K. Wohrer, A. Chetioui, A. Cassimi, J. P. Grandin, J. M. Ramillon, M. Cornille, and C. Stephan, *Phys. Rev. Lett.* **79**, 3625 (1997).
- [81] P. Woerlee, T. M. El Sherbini, F. De Heer, and F. Saris, *J. Phys. B: At. Mol. Phys.* **12**, L235 (1979).
- [82] R. Morgenstern, A. Niehaus, and G. Zimmermann, *J. Phys. B: At. Mol. Phys.* **13**, 4811 (1980).